COMMUNICATION

Check for updates

Magnetic frustration in the high-pressure Mn₂MnTeO₆ (Mn₃TeO₆-II) double perovskite†

Ángel M. Arévalo-López, [ID] *[a] Elena Solana-Madruga,[b] Cintli Aguilar-Maldonado,[a] Clemens Ritter,[c] Olivier Mentré [ID] [a] and J. Paul Attfield [ID] *[b]

A new double perovskite Mn₂MnTeO₆ has been obtained by high pressure phase transformation of a corundum-related precursor. It is antiferromagnetic below 36 K and develops a magnetic structure with magnetic moments of 4.8 μ_B and 3.8 μ_B for Mn²⁺ at the A and B sites respectively. This new polymorph accounts for a recently reported decrease in the bandgap of Mn₃TeO₆ under pressure that may lead to useful light-harvesting properties.

The ABO₃ perovskite structure has proven to be very versatile, since it can accommodate several cations at both A and B sites. The consequent accessibility to a wide range of magnetic and electrical properties have attracted much attention. Perovskites show increasing distortion with decreasing ionic radius of the A-site cation, down to tolerance factors $t = (r_A + r_O)/(\sqrt{2}(r_B + r_O))$ of 0.75, where r_A, r_B and r_O are the ionic radii of the A, B and O ions.[1] However, the use of high pressures enables small cations such as Mn²⁺ ($r = 0.96$ Å)[2] to be accommodated at the A-sites, allowing complex electronic and magnetic interactions. For example Mn²⁺V⁴⁺O₃ perovskite shows the coexistence of localized d⁵ Mn²⁺ and itinerant d¹ electron V⁴⁺ cations.[3] Further variety is achieved in high pressure double perovskites (DPvs) Mn₂BB′O₆ with ordering of two cations on the B sites; Mn₂BSbO₆ (B = Sc, Cr, and Fe),[4–6] Mn₂BReO₆ (B = Mn, Fe and Co)[7–9] and Mn₂(Fe₀.₈Mo₀.₂)MoO₆.[10]

Tellurium based oxides M₂MTeO₆ (M = Mn, Co and Ni) have structures based on the corundum arrangement at ambient pressure (see Fig. S1, ESI†) and show a variety of complex magnetic orders. Mn₃TeO₆-I crystallises in the Mg₃TeO₆-type structure.[11] Below 24 K it shows the coexistence of an elliptical helix and a sinusoidal spin density wave, both being incommensurate with the crystal structure.

a Univ. Lille, CNRS, Centrale Lille, ENSCL, Univ. Artois, UMR 8181 – UCCS – Unité de Catalyse et Chimie du Solide, F-59000 Lille, France.
E-mail: angel.arevalo-lopez@univ-lille.fr
b Centre for Science at Extreme Conditions (CSEC) and School of Chemistry, The University of Edinburgh, EH9 3FD, UK. E-mail: j.p.attfield@ed.ac.uk
c Institut Laue-Langevin, Avenue des Martyrs 71, 32042 Grenoble Cedex, France
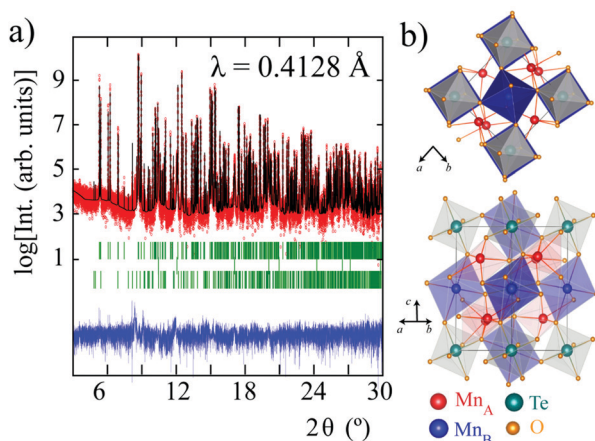† Electronic supplementary information (ESI) available: Supporting figures and tables. See DOI: 10.1039/c9cc07733b

This phase has shown a dielectric response below 21 K and so is a type-II multiferroic.[12] Co₃TeO₆ has 5 independent Co sites, providing a rich magnetic phase diagram[13] and Ni₃TeO₆ is a non-hysteretic colossal magnetoelectric material with a collinear antiferromagnetic (AFM) structure stabilised on stacked honeycomb layers.[14]

A recent study of light-harvesting properties of Mn₃TeO₆-I discovered an irreversible 39% bandgap reduction during *in situ* measurements under pressure.[15] We have explored the possibility of transforming ambient pressure Mn₃TeO₆-I phase into a recoverable double perovskite using high pressure and high temperature conditions, and we report here the new double perovskite Mn₂MnTeO₆, which is likely to be responsible for the reported bandgap engineering.

Mn₃TeO₆-I, prepared at 1270 K by the solid state synthesis method of ref. 11 was packed into a Pt capsule, pressed at 8 GPa and heated at 1173 K using a Walker-type module in a multi-anvil press. After 20 minutes, the temperature was quenched and the pressure was slowly released. Synchrotron X-ray diffraction (SXRD) powder data were collected at room temperature using the BL04 beamline at ALBA, Barcelona. Neutron powder diffraction (NPD) data were taken on 6 combined high pressure samples ($\approx$120 mg) at 50 K, 1.5 K and several intermediate temperatures using the D1B beamline at the ILL, Grenoble. Zero-field cooled and field cooled (ZFC and FC) magnetic susceptibilities and a magnetisation-field loop at 2 K were measured using a PPMS Dynacool from Quantum Design.

Preliminary laboratory X-ray diffraction evidenced the transition from Mn₃TeO₆-I into a new double perovskite, Mn₃TeO₆-II. This was found to have a monoclinic $P2_1/n$ rock-salt B-site ordered DPv structure from Rietveld fitting of 300 K SXRD data (Fig. 1a). A few % of δ-Mn₃O₄ (CaMn₂O₄-type) and Pt from the capsule are included in the refinements. The SXRD results are summarised in Table 1 and the structure is shown in Fig. 1b.

Antisite disorder between Mn_B and Te positions was checked but no mixing was found within error showing that Mn₃TeO₆-II is fully cation-ordered. The refined structural model shows that the Mn_BO₆ octahedra are distorted while TeO₆ octahedra are more regular (Table 1). Octahedral tilts $\sim 20°$ are comparable to

Fig. 1 Rietveld fit (a) of the DPv structure of Mn_2MnTeO_6 (b) from 300 K SXRD data. Second and third rows of Bragg tick marks are minor amounts of Pt from the capsule (2.2(1)%) and δ-Mn_3O_4 (1.9(1)%).

Table 1 Atomic positions and main interatomic distances and bond angles from the Rietveld fit of 300 K SXRD data. S.G. $P2_1/n$, a = 5.29370(1) Å, b = 5.45203(1) Å, c = 7.80894(1) Å, β = 89.62514(5)°

Site	x	y	z	Biso (Å^2)	Occ
Te (2a)	0	0	0	0.43(1)	0.5
Mn_B (2b)	0.5	0.5	0	0.56(2)	0.5
Mn_A (4e)	0.4887(2)	0.0475(1)	0.2397(1)	0.66(2)	1
O1 (4e)	0.1677(8)	0.2784(7)	0.0808(6)	0.31(5)	1
O2 (4e)	0.7106(8)	0.1745(8)	−0.0520(5)	0.31(5)	1
O3 (4e)	0.8794(7)	0.9244(7)	0.2215(5)	0.31(5)	1

d_{M-O} (Å)		$\langle M-O-M \rangle$ (°)	
$2\times$ (Mn_B–O1)	2.308(4)	Mn_B–O1–Te	136.2(3)
$2\times$ (Mn_B–O2)	2.133(5)	Mn_B–O2–Te	144.9(3)
$2\times$ (Mn_B–O3)	2.308(4)	Mn_B–O3–Te	137.0(3)
$\langle Mn_B$–O$\rangle$	2.249(6)		
$2\times$ (Te–O1)	1.870(5)	Mn_A–O1–Mn_B	96.5(1)
$2\times$ (Te–O2)	1.851(5)	Mn_A–O2–Mn_B	109.6(2)
$2\times$ (Te–O3)	1.885(4)	Mn_A–O3–Mn_B	98.7(1)
$\langle$Te–O$\rangle$	1.868(5)		
$2\times$ Mn_A–O1	2.188(5)	ϕ	21.5°
	2.458(5)		
$3\times$ Mn_A–O2	2.179(5)	θ	19.7°
	2.648(5)		
	2.660(5)		
$2\times$ Mn_A–O3	2.178(5)	$\Delta[Mn_BO_6]$	2.30×10^{-3}
	2.192(4)	$\Delta[TeO_6]$	1.04×10^{-4}
$\langle Mn_A$–O$\rangle$	2.358(4)		

Octahedral distortions calculated from $\Delta[MO_6] = (1/n) \times \sum (d_i - d_{av})^2/d_{av}$. Tilt angles along [001] ϕ and [110] θ are calculated from $(180 - \langle M-O-M \rangle)/2$. R_p = 16.8%, R_{wp} = 21.9%, R_f = 5.34%, R_B = 7.50%, χ^2 = 2.22%.

those for other $Mn_2BB'O_6$ double perovskites and reflect the significant distortion in agreement with the small t-value (t = 0.8) for this high pressure polymorph.

ZFC and FC magnetic susceptibilities were measured under an external field of 500 Oe (Fig. 2). They show a single antiferromagnetic transition at T_N = 36(0.5) K. A Curie–Weiss fit to the inverse susceptibility in the 100–300 K temperature range gives μ_{eff} = 5.6 μ_B/Mn^{2+}, in good agreement with the theoretical value of 5.92 μ_B for spin only Mn^{2+} (S = 5/2).
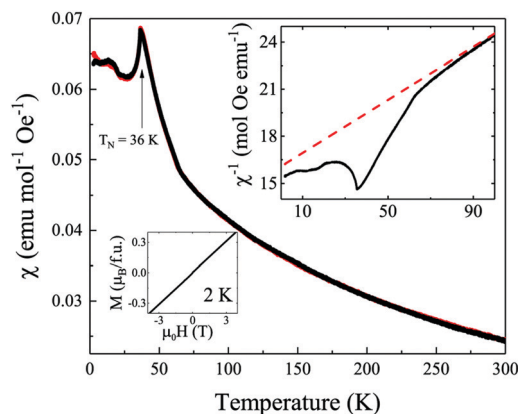

Fig. 2 ZFC (black) and FC (red) magnetic susceptibility of Mn_2MnTeO_6. Insets show the reciprocal susceptibility with C−W from high temperature (red dashed line) (right) and the field dependent magnetisation at 2 K (left).

The large negative Weiss constant θ = −183(1) K indicates predominant antiferromagnetic interactions, and the linear dependence of magnetisation on applied field at 2 K (left inset in Fig. 2), demonstrates the absence of a ferromagnetic component to the low temperature order. The upturn of the susceptibility observed below 25 K may be due to traces of the Mn_3TeO_6-I phase (T_N = 24 K).

Rietveld fits to the NPD data collected at D1B at 50 K and 1.5 K are shown in Fig. 3a. The large difference between neutron scattering lengths for Mn (−3.73 fm) and Te (5.80 fm) appear ideal to test for antisite disorder, thus the refinements confirmed the well-ordered structural model obtained from SXRD. Oxidation states estimated from BVS calculations on the 50 K NPD model are 2.1, 1.7 and 6.0 for Mn_A, Mn_B and Te sites respectively, demonstrating that the charge distribution is $Mn_2^{2+}Mn^{2+}Te^{6+}O_6$.

Prominent magnetic peaks observed below T_N can be indexed with the $k = [\frac{1}{2} 0 \frac{1}{2}]$ propagation vector. The magnetic symmetry analysis was performed using the BasIreps tool implemented in the Rietveld refinement program FullProf Suite.[16] The resulting irreducible representations (Ireps) are summarised in Table S1 in the ESI† and all four simple possible models were tested. The best fit is when both A- and B-site Mn spins follow Irep Γ_4 and can be refined independently (R_B = 6.60%, R_f = 8.54%, R_{Mag} = 10.1%, χ^2 = 1.233 for T = 1.5 K). The 1.5–50 K difference pattern containing only magnetic intensity is shown as an inset in the lower panel of Fig. 3a and magnetic refinement details are shown in ESI† and Table S2.

The magnetic structure of Mn_2MnTeO_6-II, depicted in Fig. 3b, can be described as ab layers of Mn_A spins AFM coupled with Mn_B spins perpendicular to the a direction in the magnetic unit cell. These layers are separated by diamagnetic TeO_6 octahedra, stacked AFM along the c direction and with the spins confined in the ac plane. The 90° superexchange Mn_A–O–Mn_B d^5–d^5 interactions are assumed to be the dominant ones (see Table 1), and satisfy the Goodenough–Kanamori–Anderson rules (GKA).[17] The refined ordered magnetic moments at 1.5 K converge to μ_A = 4.8(6) μ_B and μ_B = 3.9(1) μ_B for A- and B-site
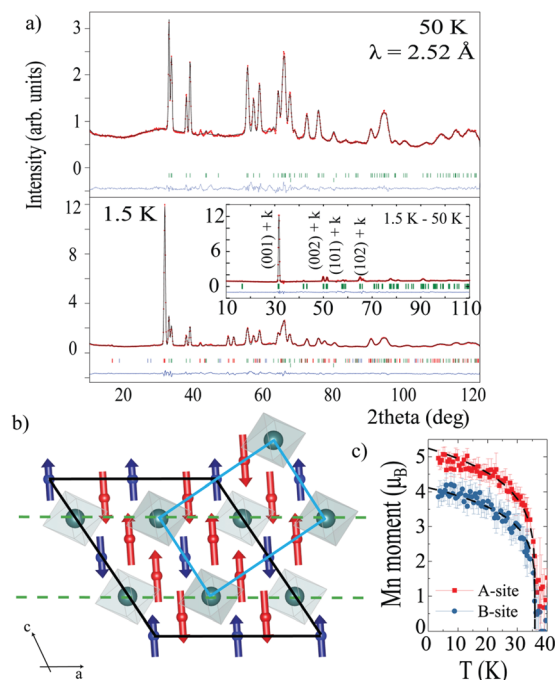
ChemComm

Fig. 3 (a) Rietveld fits of the nuclear and magnetic structures to the 50 K (top) and 1.5 K (bottom) NPD data. The right inset shows the fit of the magnetic model to the 1.5–50 K difference pattern. (b) ac plane of the magnetic structure of Mn_2MnTeO_6 with Mn_A and Mn_B spins as red and blue arrows respectively. Magnetic unit cell t is delimited with a black line and related to the crystallographic cyan one via the transformation matrix: [(1 0 −1), (0 −1 0), (−2 0 0)] with an origin shift of (0, 0, 1/2) and magnetic space group P_c2_1/n (14.80). Green dashed lines show the AFM planes described in the text. (c) Thermal evolution of the Mn^{2+} magnetic moments and fit to the critical law (dashed black line) as described.

Table 2 Main features of the magnetic behaviour for $Mn_2BB'O_6$ double perovskites, including, electronic configuration of B and B' cations, transition temperature, Weiss constant (θ), frustration index ($f = |\theta|/T_N$) and propagation vector (k)

| B | B' | d_B | | $d_{B'}$ | T_N/T_C (K) | θ | f | k |
		t_{2g}	e_g					
Sc	Sb	0	0	10	22	94	4.3	0 0 0[4]
Mn	Te	3	2	10	36	183	5.1	$\frac{1}{2}$ 0 $\frac{1}{2}$[a]
Cr	Sb	3	0	10	55	220	4.0	$\frac{1}{2}$ 0 $\frac{1}{2}$[5]
Fe	Sb	3	2	10	60	180	3.0	0 k_y 0[6]
Co	Re	5	2	1	94	26	3.6	$\frac{1}{2}$ $\frac{1}{2}$ 0[9]
Mn	Re	3	2	1	109	147	1.4	$\frac{1}{2}$ $\frac{1}{2}$ 0[7]
$Fe_{0.8}Mo_{0.2}$	Mo	3	2	1	194	50	0.3	0 0 0[10]
Fe	Re	3	2	2	520	452	0.9	0 0 0[8]

[a] This work.

Mn^{2+} respectively. The refined value for Mn_A agrees well with the expected ordered magnetic moment of 5 μ_B for Mn^{2+}, while the reduced value obtained for the Mn_B sublattice reflects some frustration present in the system, the later also supported by the ratio $f = |\theta|/T_N \sim 5$.

The magnetic model was used to fit the NPD scans at intermediate temperatures giving the evolution of the magnetic moments at both sites, as shown in Fig. 3c. Their fit by the critical law $\mu(T) = \mu(0) \times [1 - (T/T_N)]^\beta$ in the $(T_N/2) < T < T_N$ temperature range led to the parameters $T_N = 35.8(1)$ K and $\beta \approx 0.19(1)$, confirming a simultaneous order of both sublattices, in agreement with magnetisation measurements. The small β value suggests a reduced dimensionality, being close to the expected value of 0.23 for a 2D-XY model[18] and agreeing with the refined magnetic structure with spin directions confined into the ac plane.

In this context, the comparison with related high-pressure double perovskites $Mn_2BB'O_6$ is remarkable. Table 2 summarises the main features of their magnetic behaviours, which suggests the essential role of the diamagnetic B' cation on the frustrated B-site magnetic moments of these compounds as detailed below. Mn_2MnTeO_6, Mn_2MnReO_6 and Mn_2CoReO_6 are the only $Mn_2BB'O_6$ compounds reported to stabilise a DPv structure with divalent B and hexavalent B' cations. The highest magnetic frustration is observed in Mn_2MnTeO_6 and is released in

Mn_2BReO_6 by the presence of the paramagnetic cation Re^{6+}, which enables further superexchange pathways within the B sublattice and consequently increases T_N. Both Mn_2CoReO_6 and Mn_2MnReO_6 become ordered around 100 K into almost perpendicular AFM A and B sublattices with $k = [\frac{1}{2} \frac{1}{2} 0]$ and with reduced moments in B.[7,9] The isoelectronic Mn^{2+} cations at A and B sites in Mn_2MnReO_6 give rise to magnetoelastic effects that prompt Re magnetic ordering at lower temperatures than the Mn ($f = 1.4$). However, in Mn_2CoReO_6 with Co^{2+} in a high spin state, some GKA paths are blocked and it recovers some frustration increasing f up to 3.6. In Mn_2FeReO_6 the strong coupling between Fe^{3+} (d^5) and Re^{5+} (d^2) leads to a ferrimagnetic ordering on the B/B'-sites at high temperatures into a simple $k = [0\ 0\ 0]$ magnetic structure ($f = 0.9$).[8] Likewise, $Mn_2Fe_{0.8}Mo_{0.2}MoO_6$ shows almost no frustration ($f = 0.3$) due to the B-sublattice disordering of cations and the presence of Mo in a 4+ and 5+ oxidation states.

Our comparison has to include compounds of type Mn_2BSbO_6 (B = Sc, Cr and Fe) due to the presence of a diamagnetic B' cation as in Mn_2MnTeO_6. All of them achieve high degrees of magnetic frustration with transitions lower than 60 K. B = Sc, where only Mn^{2+} at the A sites are paramagnetic, has a strong frustration ($f = 4.3$) with AFM order at 22 K into a simple collinear magnetic structure with $k = [0\ 0\ 0]$.[4] B = Cr^{3+} shows the closest magnetic structure to that of Mn_2MnTeO_6, with $k = [\frac{1}{2} 0 \frac{1}{2}]$ and AFM d^5–d^3 A–O–B superexchange interactions at 90°.[5] The weaker nature of these interactions compared to the d^5–d^5 Mn_A^{2+}–O–Mn_B^{2+} of Mn_2MnTeO_6, justifies the slightly lower frustration of Mn_2CrSbO_6. Finally, Mn_2FeSbO_6 is isoelectronic to Mn_2MnTeO_6 with both Mn^{2+} and Fe^{3+} d^5 cations. Mn_2FeSbO_6 presents an incommensurate helical magnetic structure with $k = [0\ 0.426\ 0]$.[6] The origin of this difference is that the exchange integral for Fe^{3+} is much larger than that for Mn^{2+},[19] inducing strong competitions between AFM d^5–d^5 A–O–B and A–O–A interactions, thus frustrating the compound into a helical magnetic structure. In the case of Mn^{2+} the larger difference between these interactions, prevents the rotation of the spins and the release of the strong magnetic frustration, see ESI† for the interplays between A–A, B–B and A–B with frustrated topologies.
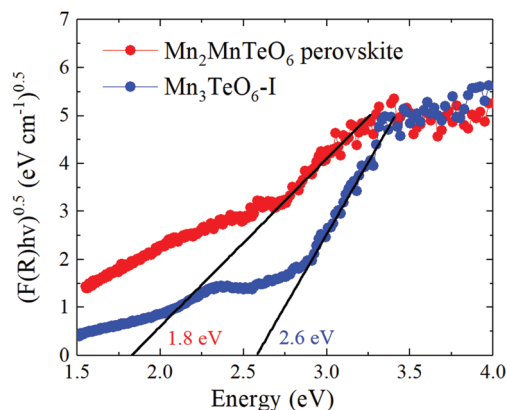
Fig. 4 Kubelka–Munk plots (for an indirect bandgap) – for Mn_3TeO_6-I and the Mn_2MnTeO_6 high-pressure double perovskite polymorph, both measured at ambient pressure and temperature.

Finally, Mn_3TeO_6 has been recently reported as a promising light-harvesting material due to an irreversible pressure-induced phase transition occurring at 16–18 GPa, where an energy band-gap reduction of $\Delta E_{gap} \approx 1$ eV is observed.[15] Our experimental plots of the Kubelka–Munk function of the UV-VIS reflectance spectra in Fig. 4 show a $\Delta E_{gap} \approx 0.8$ eV reduction from the Mn_3TeO_6 precursor (E_{gap} = 2.6 eV) to the Mn_2MnTeO_6 perovskite (E_{gap} = 1.8 eV) and we conclude that this is very probably the phase observed in the high pressure measurements. The change in connectivity from edge- to corner-shared octahedra between both polymorphs explains the decrease in the bandgap in the double perovskite.[20]

In conclusion, a new DPv Mn_2MnTeO_6 has been prepared by high-pressure high-temperature transformation of the rhombohedral polymorph. Due to the large charge and size difference between Mn^{2+} and Te^{6+}, Mn_2MnTeO_6 shows a fully ordered B/B' rock-salt type DPv structure. It is AFM below T_N = 36 K and it develops a complex magnetic structure with ordered magnetic moments of 4.8(1) μ_B and 3.8(1) μ_B at the A and B sites respectively. The magnetic structure describes AFM *ab* layers of A- and B-site spins, AFM coupled along the *c* axis, with the spins confined in the *ac* plane. Mn_2MnTeO_6 shows the highest frustration index among the A-site manganites with DPv structure. Replacement by non-magnetic B' cations proves to be a way to enhance the frustration and may be used as tuning parameter in partial B' substitutions. Formation of this DPv polymorph accounts for the previously reported bandgap reduction under pressure.

Conflicts of interest

There are no conflicts to declare.

Notes and references

1 V. M. Goldschmidt, *Mat.- Naturv. Kl.*, 1926, **2**, 117.
2 R. D. Shannon and C. T. Prewitt, *Acta Crystallogr., Sect. B: Struct. Crystallogr. Cryst. Chem.*, 1969, **25**, 925.
3 M. Markkula, A. M. Arevalo-Lopez, A. Kusmartseva, J. A. Rodgers, C. Ritter, H. Wu and J. P. Attfield, *Phys. Rev. B: Condens. Matter Mater. Phys.*, 2011, **84**, 094450.
4 E. Solana-Madruga, A. J. Dos santos-García, A. M. Arévalo-López, D. Ávila-Brande, C. Ritter, J. P. Attfield and R. Sáez-Puche, *Dalton Trans.*, 2015, **44**, 20441.
5 A. J. Dos santos-García, E. Solana-Madruga, C. Ritter, D. Ávila-Brande, O. Fabelo and R. Sáez-Puche, *Dalton Trans.*, 2015, **44**, 10665.
6 A. J. Dos santos-García, C. Ritter, E. Solana-Madruga and R. Sáez-Puche, *J. Phys.: Condens. Matter*, 2013, **25**, 206004.
7 A. M. Arévalo-López, F. Stegemann and J. P. Attfield, *Chem. Commun.*, 2016, **52**, 5558.
8 A. M. Arévalo-López, G. M. McNally and J. P. Attfield, *Angew. Chem., Int. Ed.*, 2015, **54**, 12074.
9 C. E. Frank, E. E. McCabe, F. Orlandi, P. Manuel, X. Tan, Z. Deng, M. Croft, V. Cascos, T. Emge, H. L. Feng, S. Lapidus, C. Jin, M. X. Wu, M. R. Li, S. Khalid, N. Quackenbush, S. Yu, D. Walkerk and M. Greenblatt, *Chem. Commun.*, 2019, **55**, 3331.
10 M.-R. Li, P. W. Stephens, M. Croft, Z. Deng, W. Li, C. Jin, M. Retuerto, J. P. Hodges, C. E. Frank, M. X. Wu, D. Walker and M. Greenblatt, *Chem. Mater.*, 2018, **30**, 4508.
11 S. A. Ivanov, P. Nordblad, R. Mathieu, R. Tellgren, C. Ritter, N. V. Golubko, E. D. Politova and M. Weile, *Mater. Res. Bull.*, 2011, **46**, 1870.
12 S. A. Ivanov, C. Ritter, P. Nordblad, R. Tellgren, M. Weil, V. Carolus, T. Lottermoser, M. Fiebig and R. Mathieu, *J. Phys. D: Appl. Phys.*, 2017, **50**, 085001.
13 S. A. Ivanov, R. Tellgren, C. Ritter, P. Nordblad, R. Mathieu, G. André, E. D. Politova and M. Weil, *Mater. Res. Bull.*, 2012, **47**, 63.
14 Y. S. Oh, S. Artyukhin, J. J. Yang, V. Zapf, J. W. Kim, D. Vanderbilt and S.-W. Cheong, *Nat. Commun.*, 2014, 4201.
15 L. Liu, H. Skogby, S. Ivanov, M. Weil, R. Mathieu and P. Lazor, *Chem. Commun.*, 2019, **55**, 12000–12003.
16 J. Rodriguez-Carvajal, *Phys. B*, 1993, **192**, 55.
17 J. B. Goodenough, *Magnetism and the chemical bond*, Wiley, New York, 1963.
18 A. Taroni, S. T. Bramwell and P. C. W. Holsworth, *J. Phys.: Condens. Matter*, 2008, **20**, 275233.
19 P. W. Anderson, *Solid State Phys.*, 1963, **14**, 99.
20 M. E. Kamminga, G. A. de Wijs, R. W. A. Havenith, G. R. Blake and T. T. M. Palstra, *Inorg. Chem.*, 2017, **56**, 8408.